nature materials

SUPPLEMENTARY INFORMATION

DOI: 10.1038/NMAT4715

Measuring nonlinear stresses generated by defects in 3D colloidal crystals

Neil Y.C. Lin[†],[1] Matthew Bierbaum[†],[1] Peter Schall,[2] James P. Sethna,[1] and Itai Cohen[1]

[1]*Department of Physics, Cornell University, Ithaca, NY 14853*

[2]*Institute of Physics, University of Amsterdam, Amsterdam, The Netherlands*

[†] These authors contributed equally to this work

DOI: 10.1038/NMAT4715

Contents

I. DERIVATION OF THE SALSA METHOD

A. Derivation

For a hard-sphere colloidal system, its bulk pairwise Brownian stress can be calculated by an integral over the three-dimensional pair correlation function $g(\vec{r})$ [1–4].

$$\sigma_{ij}^{B} = nk_BTa\int_{S_2}\hat{r}_i\hat{r}_j n g(\vec{r})dS_2 + nk_BT\delta_{ij} \tag{1}$$

Here, n is the number density of particles, k_BT is the thermal energy, a is the particle radius, and i, j are the indices of the stress tensor. The second term is the ideal gas stress contribution arising from the kinetic energy. The off-diagonal components of the first term, which usually dominate at high volume fractions, simply capture the anisotropy of $g(\vec{r})$ at contact surface S_2. To determine the stresses at the particle-level, we write the pair correlation function, $g(\vec{r})$, as an ensemble average of delta functions.

$$\begin{aligned}\sigma_{ij}^{B} &= \left\langle \frac{k_BTa}{\Omega}\int_{S_2}\hat{r}_i\hat{r}_j\frac{N}{V}\frac{V}{N^2}\sum_{\alpha}\sum_{\beta\neq\alpha}\delta(\vec{r}-\vec{r}^{\alpha\beta})dS_2\right\rangle + nk_BT\delta_{ij}\\ &= \left\langle \frac{1}{N}\sum_{\alpha}\frac{k_BTa}{\Omega}\int_{S_2}\hat{r}_i\hat{r}_j\sum_{\beta\neq\alpha}\delta(\vec{r}-\vec{r}^{\alpha\beta})dS_2\right\rangle + nk_BT\delta_{ij}\end{aligned} \tag{2}$$

where V, N, Ω are system volume, particle number, and particle volume, respectively. The bracket $\langle ...\rangle$ denotes an average over configurations and can be replaced with a time average in our system. In Eq. 2 we identify the outer sum as being an average over the particles in the sample, so we obtain an individual stress tensor for each,

$$\begin{aligned}\sigma_{ij}^{\alpha} &= \frac{k_BTa}{\Omega^{\alpha}}\left\langle\int_{S_2}\hat{r}_i\hat{r}_j\sum_{\beta\neq\alpha}\delta(\vec{r}-\vec{r}^{\alpha\beta})dS_2\right\rangle + nk_BT\delta_{ij}\\ &= \frac{k_BTa}{\Omega^{\alpha}}\bar{\Psi}_{ij}^{\alpha} + nk_BT\delta_{ij}\end{aligned} \tag{3}$$

The elements of the sum $\bar{\Psi}_{ij}^{\alpha}$ can be identified as the fabric tensor linear density of particle α as the units work out to be $[1/L]$. This fabric tensor density directly reports the angular distribution of neighbors in contact with a particle while the magnitude of its trace is related to the total number of neighbors. To calculate $\bar{\Psi}_{ij}^{\alpha}$ in simulation and experiment,

DOI: 10.1038/NMAT4715

it is necessary to perform an average over a narrow interval $\Delta \ll 1$

$$\begin{aligned}\bar{\Psi}_{ij}^{\alpha} &= \left\langle \int_{S_2} \sum_{\beta\neq\alpha} \hat{r}_i \hat{r}_j \delta(\vec{r}-\vec{r}^{\alpha\beta}) dS_2 \right\rangle \\ &\approx \left\langle \frac{1}{\Delta} \int_{S_2} \int_{a}^{a+\Delta} \sum_{\beta\neq\alpha} \hat{r}_i \hat{r}_j \delta(\vec{r}-\vec{r}^{\alpha\beta}) dS_2 dr \right\rangle \\ &= \frac{1}{\Delta} \left\langle \sum_{\beta\in\Delta} \hat{r}_i^{\alpha\beta} \hat{r}_j^{\alpha\beta} \right\rangle \end{aligned} \tag{4}$$

where Δ is the thickness of the measurement shell and $\hat{r}^{\alpha\beta}$ is the unit vector connecting the centers of particles α and β. Using this particular form, the SALSA formula reads

$$\begin{aligned}\sigma_{ij}^{\alpha} &= \frac{k_B T}{\Omega^{\alpha}} \left(\frac{a}{\Delta}\right) \left\langle \sum_{\beta\in\Delta} \hat{r}_i^{\alpha\beta} \hat{r}_j^{\alpha\beta} \right\rangle + n k_B T \delta_{ij} \\ &= \frac{k_B T}{\Omega^{\alpha}} \left(\frac{a}{\Delta}\right) \Psi_{ij}^{\alpha}(\Delta) + n k_B T \delta_{ij} \end{aligned} \tag{5}$$

where Ψ_{ij}^{α} can now be identified as the fabric tensor of particle α. In general, the shell thickness $\Delta \ll 1$ should be small enough that the measurement result σ_{ij}^{α} becomes independent of the particular choice of Δ. In the calibration section, we perform experiments and simulations to confirm this independence. The details concerning the particle volume Ω^{α} and converting the pointwise stresses to continuum fields are discussed in later sections.

Finally, it is possible to extend our particle-level stress calculations to other finite potentials including the depletion force [5–7], paramagnetic [8] and electrostatic [9] interactions, and soft particles [10, 11]. While similar calculations have been performed at the bulk scale [8], extending our method to these systems would allow us to further investigate their heterogeneous elastic properties.

B. Local structural anisotropy tensor

The local structural anisotropy tensor reports the instantaneous arrangement of colliding neighbors. The trace of this tensor, $\hat{r}_i \hat{r}_i$, is the total number of neighbors while the remaining terms capture the anisotropy of the collisions. As an illustration, we consider a two-dimensional case. Assuming one particle is at the origin and in contact with one other particle at an angle θ with respect to the x-axis then the fabric tensor can be written as

$$r_i r_j = \begin{bmatrix} \hat{r}_x\hat{r}_x & \hat{r}_x\hat{r}_y \\ \hat{r}_y\hat{r}_x & \hat{r}_y\hat{r}_y \end{bmatrix} = \begin{bmatrix} \cos^2\theta & \sin\theta\cos\theta \\ \sin\theta\cos\theta & \sin^2\theta \end{bmatrix}.$$

Here, the trace $\sin^2\theta + \cos^2\theta$ is always 1 and a maximum shear is achieved at four locations, $\theta = \pm 45°$ and $\pm 135°$. These directions correspond to the maximal compression and extension axes. For instance, if θ is 30°, then the trace is $(\sin^2 30°) + (\cos^2 30°) = 1$, and the shear component is $\hat{x}\hat{y} = \hat{y}\hat{x} = (\sin 30°)(\cos 30°) = \sqrt{3}/4$. Similarly, if θ is 90°, while the trace remains unity, the shear component becomes $\hat{x}\hat{y} = \hat{y}\hat{x} = (\sin 90°)(\cos 90°) = 0$.

C. From pointwise functions to continuum fields

In the literature of molecular dynamics simulation, the virial

$$s_{ij}^{\alpha} = \frac{1}{2}\sum_{\beta\neq\alpha}\frac{\partial V(r)}{\partial r}\frac{r_i r_j}{r} + m v_i v_j \tag{6}$$

has been widely used to report stresses at the atomic level [12–14]. In particular, this quantity has been used to measure many interesting phenomena including the stress correlation length in liquid metals [13] and stress fluctuations near grain boundaries [14]. While the sum of the virials s_{ij} divided by system volume V yields the bulk stress of the system, there are multiple choices that can be made as to how to incorporate local volume variation and how to smooth the pointwise stress into a continuum field. Similar to the Irving-Kirkwood-Noll procedure, which constructs continuum fields from the underlying discrete distribution with phase averaging, we perform a spatial average to obtain a macroscopic measurement at the particle-level [15]. The final continuum stress field $\sigma_{ij}^{cont}(\vec{x};t)$ is given by

$$\sigma_{ij}^{cont}(\vec{x};t) = \int_{\vec{y}\in\mathbb{R}} w(\vec{y}-\vec{x})\sigma_{ij}^{pt}(\vec{x};t)d\vec{y} \tag{7}$$

where $w(\vec{r})$ is a weighting kernel function, and $\sigma_{ij}^{pt}(\vec{x};t)$ is the pointwise function. Here, the weighting function w must be normalized so that the total energy is conserved during spatial averaging. We use a normalized Gaussian function that weights values closer to $\vec{x}$ more strongly than other points that are further away:

$$w(r) = \pi^{-3/2} r_w^{-3} e^{-\frac{r^2}{2r_w^2}} \tag{8}$$

DOI: 10.1038/NMAT4715

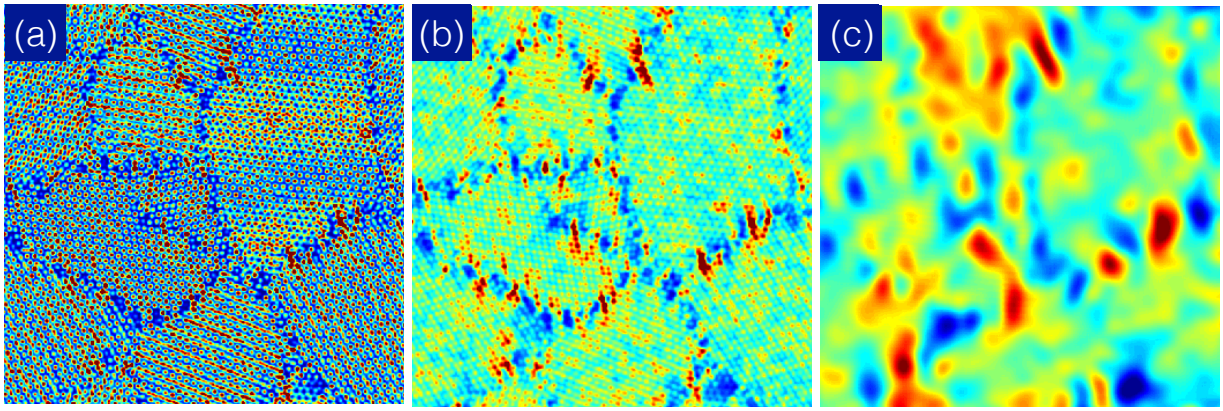

FIG. 1: **Spatially smoothed stress fields of a simulated polycrystal** We plot the smoothed stressed field of a polycrystal as a function of filter size $r_w/2a$ at (a) 0.2 (b) 0.3 and (c) 1. For small $r_w/2a$, only the points containing particle centers with assigned stresses have nonzero values. As the value of $r_w/2a$ increases, the stress field becomes smoother and more continuous. Note that since the weighting Gaussian function is normalized, the overall stress of the system is the same for all different $r_w/2a$. The color scale is adjusted for each sub figure to emphasize the stress variation features. In all calculations, we use the value $r_w/2a = 1$, where the features of individual particles are no longer distinguishable.

where $r = \|\vec{r}\|$, and the filter size r_w is chosen to emphasize the length scale of the continuum fields of interest [15]. Similar smoothing algorithms have been implemented in previous literature [16–19].

In our experiments and simulations, we set $r_w/2a = 1$ so that we remove stress features on length scales smaller than a particle. The pointwise stress is constructed by first assigning calculated particle virial, $\sigma_{ij}^{\alpha}\Omega^{\alpha}$ to their corresponding grid boxes, then dividing their values by the box volume. This pointwise function shows singularities at particle centers and zero elsewhere. Finally, we smooth the field using the Gaussian kernel, Eq. 8. We show the spatial averaged continuum fields of a simulated polycrystal for three different filter sizes r_w in Fig. 1.

In this spatial averaging procedure, the influence of local volume variation on the stress distribution is already incorporated. In particular, as the occupied volume of a particle increases, the stress is proportionally reduced due to the increased effective averaging volume. Furthermore, the final fields are nearly independent of the grid size and the mean stresses

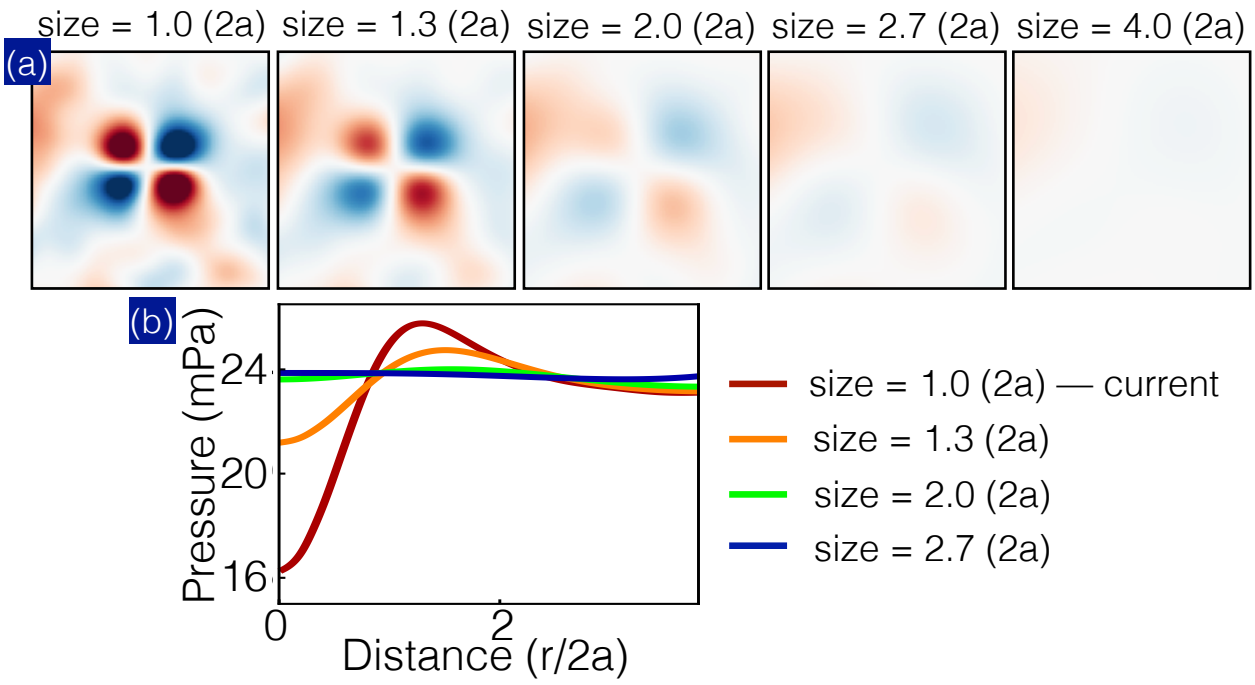

FIG. 2: **Spatially smoothed stress fields of a vacancy.** (a)The values of smoothing length scale r_w from left to right are 1.0×2a, 1.3×2a, 2.0×2a, 2.7×2a and 4.0×2a, respectively. (b) The radial distribution of pressure for different r_w.

are constant at all values of r_w.

To explore how the filter size r_w affects our final SALSA stress fields, we show the experimental vacancy stress field, σ_{xy} for five different values of r_w in Fig. 2(a). We find that the feature of the stress quadrupole [45] remains discernible up to $r_w = 2.7(2a)$. Note in Fig. 2(a), while the quadrupole distribution theoretically diverges as $1/r^3$, it is cut off by the lattice and smoothed over the distance r_w, squelching the stress features near the vacancy core. Similarly in Fig. 2(b), we find that the near field of the pressure is strongly affected by the filter, but the long-range nonlinear pressure ring at $r_w = 1(2a)$ and $1.3(2a)$ match each other. Indeed, the long-range stresses from all defects have correspondingly slow variations, and hence will be invariant to the choice of r_w. The filter size choice is a balance – hiding noise at lengths $r < r_w$ to enhance features of size $r > r_w$.

In terms of elastic theory, the filter size can be thought of a regularization for the theory, renormalizing higher order terms in the elastic free energy. To see how smoothing affects

DOI: 10.1038/NMAT4715

these terms, consider how smoothing changes a linear elastic free energy

$$\mathcal{F}_0 = \int d^3r \, S_{ijkl} \, \sigma_{ij} \, \sigma_{kl} \tag{9}$$

where S_{ijkl} is the elastic compliance tensor and σ_{ij} is the stress tensor. If we smooth the stress tensor using a Gaussian kernel of size r_w this linear elastic theory changes to

$$\begin{aligned}
\mathcal{F}' &= \int d^3r \, d^3k \, d^3k' \;\; S_{ijkl}[\sigma_{ij}(\vec{k})e^{-k^2r_w^2/2}e^{i\vec{k}\cdot\vec{r}}][\sigma_{kl}(\vec{k}')e^{-k'^2r_w^2/2}e^{i\vec{k}'\cdot\vec{r}}] \\
&= \int d^3k \;\; S_{ijkl} \, \sigma_{ij}(\vec{k}) \, \sigma_{kl}(-\vec{k}) \, e^{-k^2r_w^2} \\
&\approx S_{ijkl} \int d^3k \;\; (1 - k^2r_w^2) \, \sigma_{ij}(\vec{k}) \, \sigma_{kl}(-\vec{k}) \\
&= \int d^3k \;\; S_{ijkl} \, \sigma_{ij}(\vec{k}) \, \sigma_{kl}(-\vec{k}) - \int d^3k \;\; S_{ijkl} \, k^2r_w^2 \sigma_{ij}(\vec{k})\sigma_{kl}(-\vec{k}) \\
&= \mathcal{F}_0 - r_w^2 \int d^3k \;\; S_{ijkl}(k_m\sigma_{ij}(\vec{k}))(k_m\sigma_{kl}(-\vec{k}))
\end{aligned}$$

What new terms must we add to $\mathcal{F}'$ to cancel the second term? Since each factor of k introduces a gradient, we can check that a stress gradient term $S_{ijkl}\partial_m\partial_m\sigma_{ij}\sigma_{kl}$ has the correct form.

$$\begin{aligned}
S_{ijkl} \int d^3r \;\; \partial_m\partial_m(\sigma_{ij} \, \sigma_{kl}) &= S_{ijkl} \, \partial_m\partial_m \int d^3r \, d^3k \, d^3k' \;\; e^{-i\vec{k}\cdot\vec{r}}\sigma_{ij}(\vec{k}) \, e^{-i\vec{k}'\cdot\vec{r}}\sigma_{kl}(\vec{k}') \\
&= -2S_{ijkl} \int d^3r \, d^3k \, d^3k' \;\; k_mk'_m e^{-i\vec{k}\cdot\vec{r}}\sigma_{ij}(\vec{k}) \, e^{-i\vec{k}'\cdot\vec{r}}\sigma_{kl}(\vec{k}') \\
&= -2S_{ijkl} \int d^3k \;\; k_mk_m\sigma_{ij}(\vec{k})\sigma_{kl}(-\vec{k})
\end{aligned}$$

Indeed, the energy regularized by smoothing by r_w is the original free energy plus a filter size-dependent term times a stress gradient energy:

$$\mathcal{F}' \approx \mathcal{F}_0 + \frac{r_w^2}{2} S_{ijkl} \int d^3r \;\; \partial_m\partial_m(\sigma_{ij} \, \sigma_{kl}) \tag{10}$$

Similarly, nonlinear and other terms in the energy will produce regularization-dependent counter terms. We will now demonstrate that these gradient terms contribute less to the free energy than other nonlinear terms in the case of hard sphere crystals.

Let us consider the long and short wavelength behavior of the first nonlinear and gradient terms of the elastic free energy to see which dominates the behavior both close and far from a defect. For isotropic elasticity, the allowed terms that arise in the free energy density are

$$\mathcal{F} = C_{ijkl}\epsilon_{ij}\epsilon_{kl} + D_{ijklmn}\epsilon_{ij}\epsilon_{kl}\epsilon_{mn} + E_{ijklmn}\partial_i\partial_j\epsilon_{kl}\epsilon_{mn} \tag{11}$$

where the allowed elements of the elastic constant tensors C, D, and E are determined by the symmetries of the system being studied. In the case of isotropic materials, these tensors must be built using terms that are formed by δ_{ij} and Δ_{ijkl} and $\mathcal{D}_{ijklmn}$, the Kronecker delta and the four and six index equivalents of the Kronecker delta. That is, the parts of the free energy may be written

$$\mathcal{F}_C = c_0\,\epsilon_{ii}\epsilon_{jj} + c_1\,\epsilon_{ij}\epsilon_{ij}$$
$$\mathcal{F}_D = d_0\,\epsilon_{ii}\epsilon_{jj}\epsilon_{kk} + d_1\,\epsilon_{ij}\epsilon_{ij}\epsilon_{kk} + d_2\,\epsilon_{ij}\epsilon_{jk}\epsilon_{ki}$$
$$\mathcal{F}_E = e_0\,\partial_i\partial_i\epsilon_{jj}\epsilon_{kk} + e_1\,\partial_i\partial_j\epsilon_{ij}\epsilon_{kk} + \cdots$$

Which terms should we keep to describe the elastic fields? We consider their contributions in the case of the elastic field of a vacancy defect – since the displacement field for linear theory goes as $u(r) \sim \Delta V/r^2$, the strain field goes as $\epsilon \sim \Delta V/r^3$. The quadratic term then has energy density which scales as r^{-6}, while the nonlinear cubic term (ϵ^3) scales as r^{-9} and the gradient term as $r^{-1}r^{-1}r^{-3}r^{-3} = r^{-8}$. For short range behavior, the nonlinear contributions are nearly equal, with the cubic term contributing more for $r \ll 1$. However, we also need to consider the magnitude and scaling of the coefficients for each term. In the case of the cubic elastic constants, we know from the equation of state that the pressure diverges at maximal packing as $P \sim (\phi_c - \phi)^{-1}$, implying that e.g. the bulk modulus diverges as $K = \phi\frac{\partial P}{\partial \phi} \sim (\phi_c - \phi)^{-2}$ [20]. If we write the scaling in terms of the two length scales in the problem, the lattice constant a and the surface to surface distance Δ, we find that the cubic term in the free energy goes as $(a/\Delta)^{-2}r^{-9}$ and the first gradient term as a^2r^{-8}. In the case $(a/\Delta) \ll 1$, we find that the cubic terms dominates the gradient contributions. It is for this reason as well as the fact that gradient terms are not unique in our smoothing scheme that we only consider nonlinear elasticity without gradient terms.

II. CALIBRATION OF THE SALSA METHOD

To validate our SALSA measurements, it is crucial to calibrate the method and evaluate its performance and dependence on input parameters. We divide the calibration section into three parts: A) comparison with simulation stresses, B) contact criteria dependence, and C) force balance in a smoothed field. We show that the SALSA method accurately captures the stress fields as calculated by Brownian dynamics very well. The stress field

DOI: 10.1038/NMAT4715

determined by using SALSA is not significantly sensitive to the particle contact criteria e.g. the shell thickness Δ. Finally, we discuss a systematic residual force within the vacancy core in the continuum stress field due to the smoothing process and compare the elastic fields to similarly smoothed continuum calculations.

A. Calibration: SALSA versus actual stress

To evaluate how well SALSA is able to report the correct stress field of a complex system, we use Brownian dynamics (BD) to generate a vacancy in a simulated crystal, whose orientation is matched to that found in our experiments. We use SALSA to determine all six independent stress components and compare their values with the BD stress calculation using the same set of position data (see Fig. 3). The continuum stress field from BD is constructed by spatially averaging pointwise virials $F_i x_j$. We see that the BD and SALSA stresses exhibit a good match. We also find that SALSA stresses become more quantitatively similar to the actual stress fields as a longer time-average is performed (not shown).

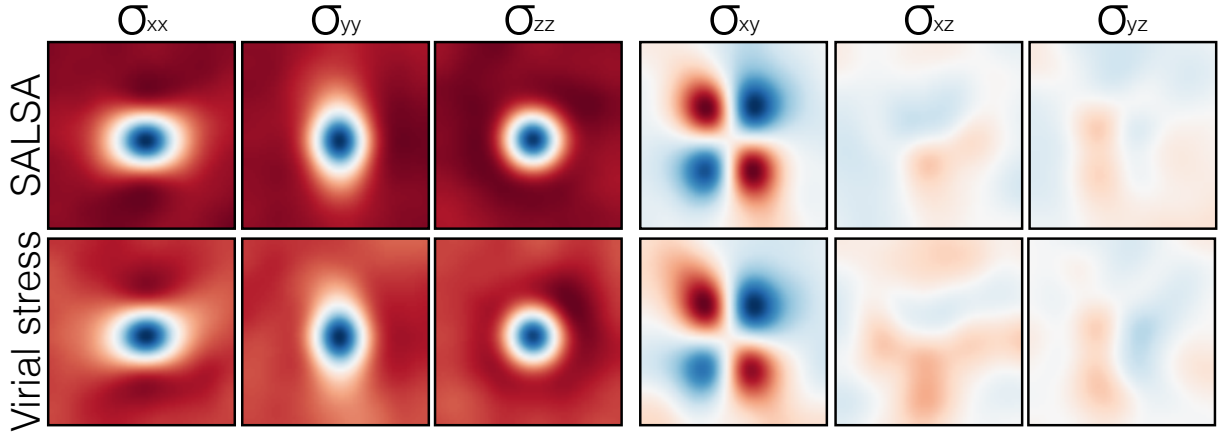

FIG. 3: **SALSA and actual stresses comparison.** Stresses determined through the SALSA method (top row) are compared with the stresses directly calculated in simulation (bottom row) using the same dataset.

B. Calibration: Contact criteria dependence

There is another parameter in the SALSA method, which is the shell thickness Δ used to identify particles in contact. This shell thickness directly determines the number of particles

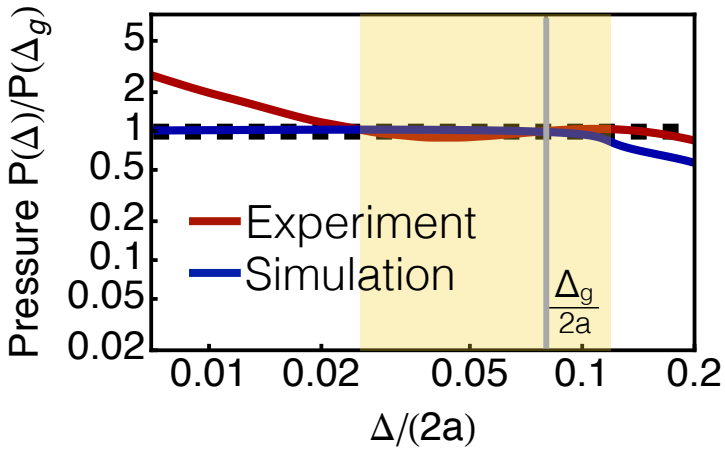

FIG. 4: **SALSA pressure versus Δ in experiment and simulation**. Pressure measured using different shell thickness Δ is plotted as a function of Δ. The pressures values P(Δ) are normalized by P(Δ_g) where $\Delta_g + 2a$ is the position of the $g(r)$ first peak, which is denoted by the gray line. The vacancy experimental data (red curve) shows that SALSA method generates quantitatively consistent results in a wide range of shell thickness $0.03(2a) \leq \Delta \leq 0.15(2a)$ (shaded area). The corresponding length scale of this thickness range is 40 nm $\leq \Delta \leq$ 230 nm. The simulation data (blue curve) demonstrate an even wider pressure plateau that extends beyond $\Delta \sim 10^{-4}(2a)$. The diverging trend of the experimental pressure at small Δ occurs due to slight particle overlaps arising from featuring uncertainties.

that are included in the stress calculation, larger Δ allowing for shorter time averages. However, at large Δ, the radial distribution of particles $g(r)$ will vary through out the thickness of the shell, leading to systematic errors in stress. We test for the optimum by calculating the pressure of a system versus $\Delta/2a$. Fig. 4 shows the SALSA pressure $P(\Delta)/P(\Delta_g)$ versus $\Delta/2a$ for both experimental and simulation data. Here, $\Delta_g/2a$ (gray line in Fig. 4) is the cutoff thickness used throughout our analysis of the experiments, where $2a + \Delta_g$ roughly coincides with the first peak of $g(r)$. We find that the measured pressure has negligible dependence on $\Delta/2a$ for $\Delta/2a \leq 0.12$. In the experiment the normalized pressure deviates from 1 when Δ is smaller than $\sim 3\%$ of the particle size, corresponding to $\approx 1/4$ of a pixel ($\sim$ 35 nm). This trend arises due to particle overlaps from featuring uncertainties. Overall, as shown in Fig. 4, both the experimental and simulation results indicate an insignificant correlation between the SALSA pressure and shell thickness Δ in

DOI: 10.1038/NMAT4715

the range of 35 nm $\leq \Delta \leq$ 230 nm (yellow shaded area).

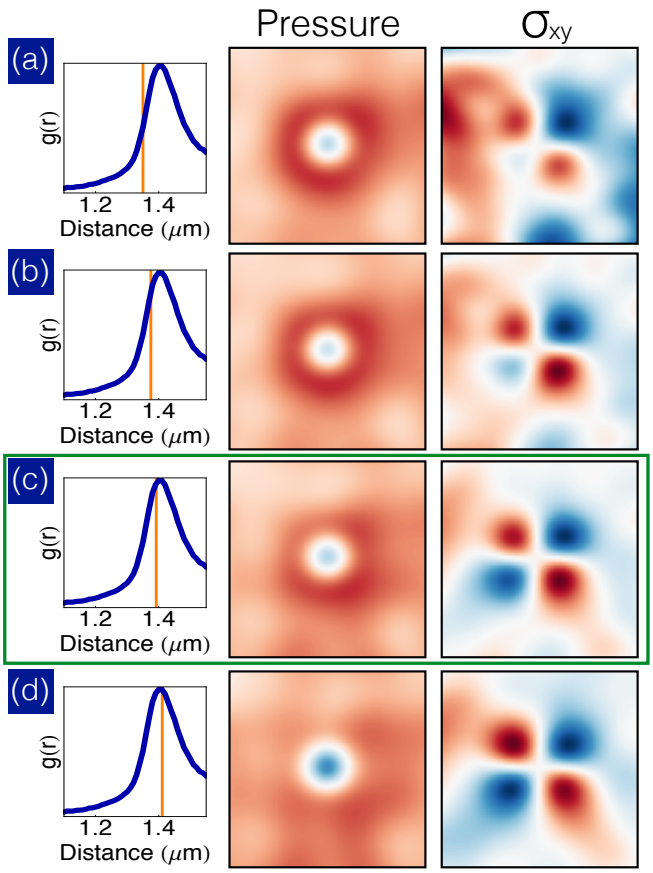

FIG. 5: **Pressure and σ_{xy} fields for different** Δ Pressure (middle row) and shear stress σ_{xy} (right row) distributions for four different values of shell thicknesses. (c) The contact criteria used throughout our experiments. The pair correlation functions $g(r)$ (left row) are plotted to illustrate the differences between the shell thickness Δ choices (orange lines).

Finally, we also investigate how the shell thickness Δ affects the spatial distribution of stresses. We show the experimental pressure and σ_{xy} fields near a vacancy for four different Δ in Fig. 5. Again, we find that the stress fields for all Δ demonstrate qualitatively similar trends, where the pressure exhibits an enhancement surrounding the defect core and σ_{xy} shows a quadrupole distribution. This weak Δ dependence is consistent with the previous experimental studies [21, 22] where the authors have found that different contact criterion consistently generate similar bulk Brownian stresses. Here, we provide a similar calibration but at the particle level. As shown in Fig. 5, it is remarkable that SALSA is able to produce consistent results with a wide range of shell thickness 35 nm $\leq \Delta \leq$ 150 nm. This wide

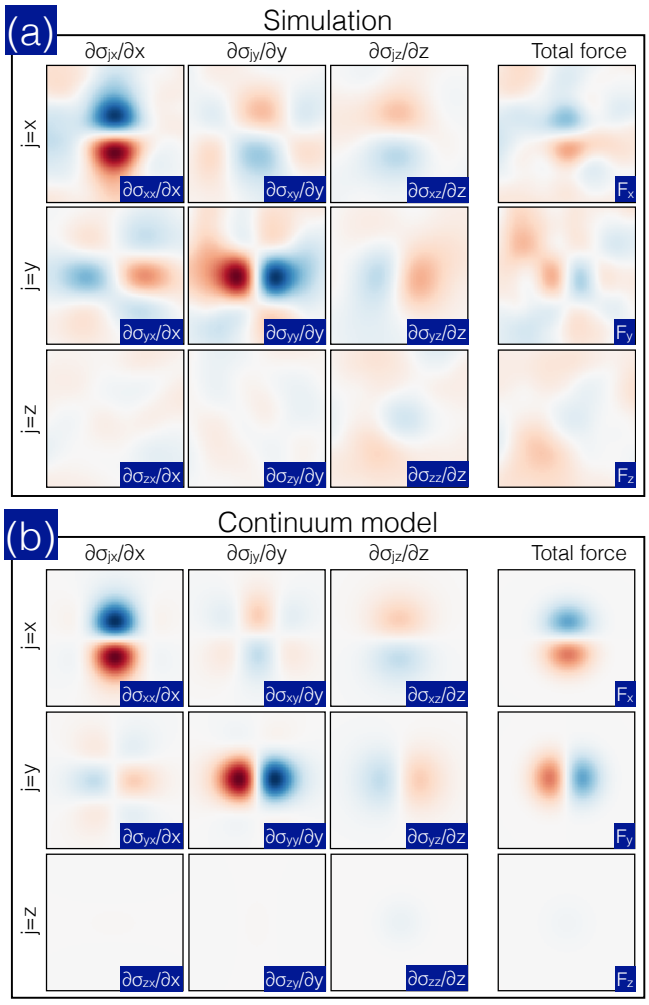

FIG. 6: **Force balance of vacancy.** The right-most frames show the divergence of the stress fields from simulation (a) and continuum theory (b). In the group of nine panels in each of these subfigures, we show the components of the divergence of the stress. Summing along each row, we find the total force as the sum of the gradients. Both the BD simulation and continuum elastic fields show systematic force dipoles in their center indicating that the small residual forces are produced not from the SALSA method but from the choices made in creating a continuum field.

window of Δ choice promises robust stress measurements in the typical colloidal experiments with 3D imaging, where the particle positions can be precisely determined with a sub-pixel resolution (≤ 50 nm) using standard featuring algorithms.

DOI: 10.1038/NMAT4715

C. Calibration: Mechanical equilibrium of a smoothed field

In principal, it is possible to further determine the continuous force field by calculating the divergence of the smoothed stress distribution. In our experiments, where all the studied regions are stationary, the calculated force field should be zero implying a mechanical equilibrium. It has recently been shown that this mechanical equilibrium of the microscopic stress closely depends on the details of the stress definition at particle-level [23]; it is important to check it for SALSA. To investigate this issue, we calculate the divergences of the vacancy SALSA stresses in simulation (Fig. 6 (a)). We find that the force fields are consistent with zero everywhere except the region of the defect core, where the force shows a dipole distribution in all components. Since there is no particle in the region that violates mechanical equilibrium, it is unclear whether this force imbalance leads to a particle drift or not. Nevertheless, to confirm that this is only a result of the smoothing procedure, we perform a similar analysis on calculated continuum elastic fields. In doing so, we mimic the SALSA measurements by introducing a pressure hole in the center, and smooth the stress fields with the same kernel used in the simulation. As shown in Fig. 6 (b), the force fields from continuum theory also display force dipoles consistent with SALSA and BD stress fields. This consistency clearly indicates that the force imbalance mostly arises from the pressure drop and smoothing algorithm rather than the SALSA calculation.

To further characterize the magnitude of the force imbalance, we perform a similar mechanical equilibrium calibration in a simulated polycrystal. In particular, we construct a three dimensional box enclosing a grain boundary. Then we determine the net force acting on this box by calculating the tractions from stresses. We find that the forces correspond to the shear and normal tractions approximately cancel each other, indicating a good mechanical equilibrium. The residual force can then be related to a drift arising from this force imbalance given that the system is over-damped. Finally, we find that the drift, which is independent of the box size, is less than 5% of the particle diameter over the entire simulation.

III. VACANCY STRESS FIELDS

A. Experimental details

We create a colloidal crystal consisting of 1.3 μm diameter silica particles via sedimentation in a sealed sample cell. The particles are suspended in a water-glycerol mixture with a refractive index matching the silica particles. This matched refractive index allows us to acquire confocal images of the sample. Vacancy defects form spontaneously during sedimentation (along with stacking faults and grain boundaries), and are imaged directly using a high-speed confocal microscope. In the measurements, we select isolated vacancies that contain no other defects within five lattice spacings in the plane or in either of the adjacent layers perpendicular to the plane.

Since the system is thermal, it is important to perform a time average to correctly determine the equilibrium stress field. Therefore, we record, analyze, and average the stress fields over 60 snapshots (20 seconds). We further average the stress field over 20 vacancies to reduce the effects of polydispersity and the local vacancy environment. In Fig. 7, we show the confocal images of all measured vacancies in the experiment (the horizontal slices of full 3D confocal image stacks) to illustrate the vacancy morphology. As shown in Fig. 7, the independent vacancies have random orientations with respect to the microscope and must be aligned before averaging. With all images aligned in the same orientation, we then calculate the stress field of each sample and average over 20 seconds. This time interval is sufficiently long for the colloids to explore the local phase space as the time required to diffuse one particle separation (100 nm) in the absence of obstructing neighbors is about 0.35 s. Finally, we average the per-vacancy stress field over all 20 samples.

Since SALSA solely relies on the particle positions to determine the stress field, the correctness of final measurements directly depends on the accuracy of particle featuring and noise in the experiment. We employ both time and sample averages to remove noise and improve such measurement accuracies. Uncorrelated noise such as the current noise in the electronics, can be effectively reduced by using a time average. On the other hand, there is correlated noise that result in a persistent featuring bias in time, including spherical aberration in the optics [24–26], the microscope point-spread-function [27–29], and particle polydispersity [30]. In the vacancy experiment, we minimize the effects of spherical aber-

DOI: 10.1038/NMAT4715

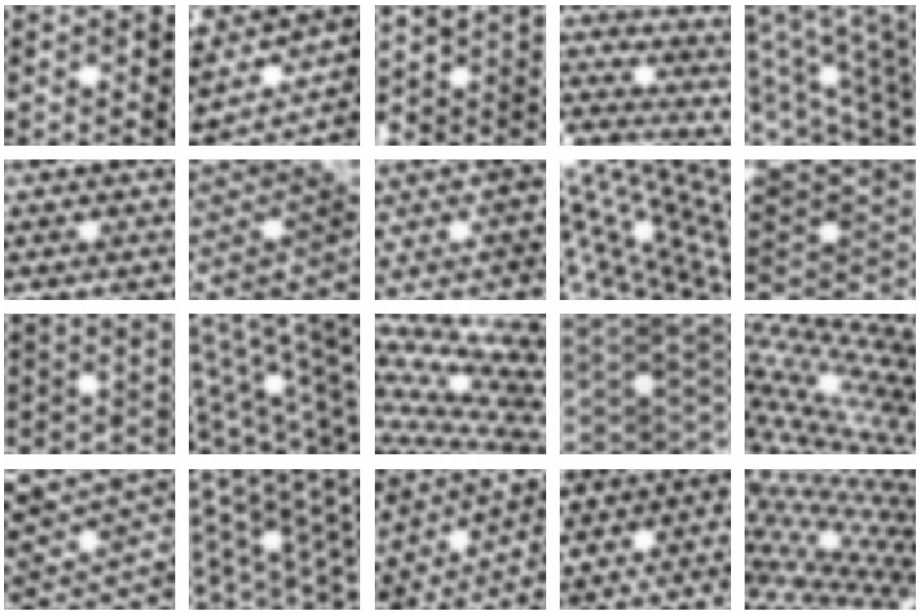

FIG. 7: **Confocal images of 20 isolated vacancies**.

ration and point-spread-function by index-matching the sample within 0.1% and confining the imaging field to a few particles away from the coverslip. Polydispersity also affects our ability to determine which particles are in contact. For instance, when two larger particles are touching, the SALSA method may identify them as not in contact because their center-to-center distance is larger than $2\langle a\rangle + \Delta$, the mean distance between particles plus the shell thickness. The polydispersity ($\approx$ 35 nm for our silica colloids) is about 30% of the shell thickness $\Delta = 106$ nm used in our experiment. In the vacancy experiment, by averaging the stress field over 20 different samples, the collision uncertainty due to polydispersity is further reduced by a factor of $\sqrt{20} = 4.5$.

Furthermore, we find that the polydispersity has different effects on the pressure and shear stress measurements. We show two representative stress components σ_{xx} and σ_{xy}, first time averaged, Fig. 8 (a) and (b), and then with an additional sample average, Fig. 8 (c) and (d). We find that the pressure does not fully capture the enhanced stress ring around the vacancy defect if only a time average is applied. However, the shear component of the same time-averaged data already shows a clear quadrupole structure that is very similar to the one with additional sample averaging. This finding implies that while the pressure measurement may rely on a more precise identification of touching particles, the shear measurement is relatively robust and insensitive to the noise. In contrast to the normal

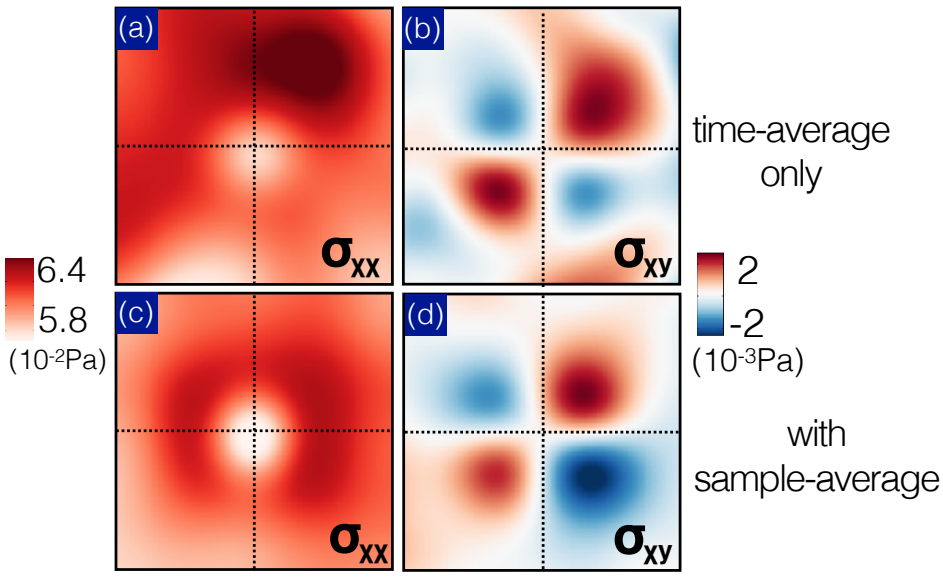

FIG. 8: **Effects of sample average**. Comparison of time average and sample average on a normal component σ_{xx} (a,c) and shear component σ_{xy} (b,d). We see that sample average improves the measurement of the normal component more than the shear components due to the effects of polydispersity.

stresses that are strongly associated with the collision (touching) probability of surrounding particles, the shear components are more related to the angular anisotropy of the neighboring particle configurations. Finally, it is also possible to avoid the effects of polydispersity by determining the individual particle size and taking the size variation into account [31].

B. Simulated vacancy stresses

We confirm the experimental findings by simulating the stress of a vacancy in a colloidal crystal using nearly hard-sphere Brownian dynamics. Here, we numerically simulate the Langevin dynamics of N particles interacting through a very sharp radial potential $V(r)$. We do so using cell neighbor lists calculated on an NVIDIA GPU integrating with the velocity Verlet algorithm. The virials of each particle, calculated through Eq. 6, are used to compare directly to the stresses calculated with the SALSA method.

Based on previous literature [22], we have tried several interparticle potentials including the Yukawa potential, pure power law, and smoothed power law. Here we use the smoothed

DOI: 10.1038/NMAT4715

power law to ensure continuity in derivatives:

$$V(r) = \mathcal{E}\left(\frac{r}{r_0} - 1\right)^2 \left(\frac{r_0}{r}\right)^{24} \tag{12}$$

To simulate the vacancy, we begin with a periodic cell of a fcc crystal with the same physical parameters as the experimental setup. We create a periodic cell containing $2^{14} = 16384$ particles at a packing fraction of $\phi = 0.59$, temperature $T = 300\, k_B T$ and viscosity $\eta = 10^3$. We remove the center particle and simulate for 2500 snapshots where each snapshot is separated by $t = 10\tau$ diffusion times. The stress of these particle configurations is calculated using both the simulation virial and SALSA and averaged over the entire simulation time. A direct comparison of these stress fields can be found in Fig. 3. We do find some quantitative differences between the experiment and simulation. For example, the pressure of the simulated vacancy is plotted as a function of distance from the defect core in Fig. 9. While the morphology in each individual stress component is very close to that seen in experiments, we do not find as strong of a pressure enhancement around the simulated vacancy. This softening is most likely due to the softened core of the potential we use. Overall, however, all the qualitative features are reproduced in each of experiment, simulation, and theory.

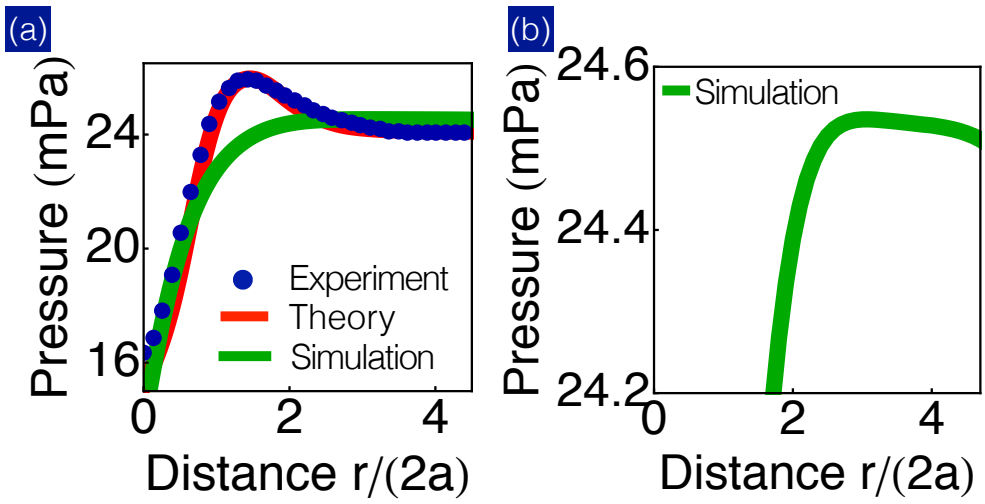

FIG. 9: **Vacancy pressure distribution** Comparison of experimental (blue dots in (a)), theoretical (red line in (a)), and simulation (green line in (b)) pressure. Despite its relatively insignificant feature, the simulated vacancy pressure also exhibits a pressure enhancement at $r \sim 4$a. All individual stress components in experiment, theory, and simulation show qualitatively similar results.

C. Continuum elastic theory

1. *Linear elasticity*

To further measure the performance of SALSA, we also compare the stress fields calculated in simulation and experiment to the corresponding continuum elastic theory. In linear isotropic elastic theory, a vacancy's displacement field can be described by a radial function determined entirely by the local volume change $u_i(r) = \Delta V/r^2\ \hat{r}_i$. This can be seen by looking at the elastic free energy which can be written

$$\mathcal{F}_{\text{linear}} = \frac{1}{2}K\epsilon_{ii}^2 + \mu(\epsilon_{ij} - 1/3\ \delta_{ij}\epsilon_{ll})^2 \tag{13}$$

where K is the bulk modulus, μ is the shear modulus and ϵ_{ij} the strain tensor, the symmetrized Jacobian of the displacement field u, $\epsilon_{ij} = 1/2(\partial_i u_j + \partial_j u_i)$. Since the material is isotropic, we make u a radial function such that $u_i(\vec{r}) = u(r)\hat{r}_i$. We then minimize the free energy with respect to this displacement field through the Euler-Langrange equations $\frac{\partial F}{\partial u_i} - \frac{\partial}{\partial x_i}\frac{\partial F}{\partial \partial u_i} = 0$, giving a differential equation for the displacement $r^2u'' + 2ru' - 2u = 0$ whose solution is given by

$$u(r) = \frac{\Delta V}{4\pi r^2} + \frac{P_\infty}{3K}r \tag{14}$$

Here, ΔV is the local volume change, P_∞ is the pressure at long length scales due to boundary conditions and K is again the bulk modulus. This displacement field leads to a strain and stress field in linear elasticity that has the form

$$\begin{aligned}
\epsilon_{ij} &= \frac{1}{2}(\partial_i u_j + \partial_j u_i) \\
&= \frac{u}{r}\left(\delta_{ij} - \frac{r_i r_j}{r^2}\right) + u'\frac{r_i r_j}{r^2} \\
\sigma_{ij} &= K\epsilon_{ll}\delta_{ij} + 2\mu(\epsilon_{ij} - 1/3\delta_{ij}\epsilon_{kk}) \\
&= K\left(2\frac{u}{r} + u'\right)\delta_{ij} + 2\mu\left(\frac{u}{r} - u'\right)\left(\frac{1}{3}\delta_{ij} - \frac{r_i r_j}{r^2}\right)
\end{aligned}$$

Using this stress field, we find the pressure field is a constant

$$P = \sigma_{ii}/3 = K\left(2\frac{u}{r} + u'\right) = P_\infty \tag{15}$$

DOI: 10.1038/NMAT4715

2. Geometric nonlinearity

However, both the simulation and experimental data show a pressure ring that suggests we need to move to higher order elasticity to accurately describe the stress field of the colloidal vacancy. The first natural attempt to capture this ring can be done by including the geometric nonlinearity (also known as finite strain), an extra term in the strain field that makes it rotationally invariant but is higher order in displacement. Doing so, we find that

$$\begin{aligned}\epsilon_{ij} &= \frac{1}{2}(\partial_i u_j + \partial_j u_i + \partial_i u_k \partial_j u_k) \\ &= \frac{u}{r}\left(\delta_{ij} - \frac{r_i r_j}{r^2}\right) + u'\frac{r_i r_j}{r^2} + \frac{1}{2}\left[\left(\frac{u}{r}\right)^2\left(\delta_{ij} - \frac{r_i r_j}{r^2}\right) + u'^2\frac{r_i r_j}{r^2}\right] \\ &= \bar{U}\left(\delta_{ij} - \frac{r_i r_j}{r^2}\right) + \bar{U}'\frac{r_i r_j}{r^2}\end{aligned}$$

where we can define $\bar{U} = u/r + 1/2(u/r)^2$ and $\bar{U}' = u' + 1/2u'^2$. We then calculate the stress which is linear in the strain, arriving at the same answer as previously, except with these variables substituted. Lastly, we find the differential equation for the radial displacement field via the Euler-Lagrange equations, yielding a long nonlinear ODE, which we omit for brevity. Fitting the experimental data using this form yields a small pressure enhancement which cannot be tuned to quantitatively match the experimental data without resorting to unphysical values for the bulk and shear modulus.

3. Nonlinear elasticity

Motivated by arguments made in Section II, we next calculate the stress field incorporating the leading terms in nonlinear isotropic elastic theory. In particular, we modify the free energy such that

$$\mathcal{F}' = \mathcal{F}_{\text{linear}} + \frac{\alpha}{3}\epsilon_{ii}\epsilon_{jj}\epsilon_{kk} + \frac{\beta}{6}\epsilon_{ij}\epsilon_{jk}\epsilon_{ki} + \frac{\gamma}{4}\epsilon_{ii}\epsilon_{jk}\epsilon_{jk} \tag{16}$$

We insert the definition of finite strain into the new free energy to arrive at another

differential equation for the displacement field as a function $u(r)$.

$$
\begin{aligned}
&r^5(24r(\lambda+2\mu)u''(r)+6(\alpha+\beta+\gamma)u'(r)^5\\
&+4u'(r)^3(2(8\alpha+3(4\beta+2\gamma+\lambda+2\mu))+15r(\alpha+\beta+\gamma)u''(r))\\
&+4u'(r)^2(8\alpha+6(2\beta+\gamma+4\lambda+6\mu)+9ru''(r)(2\alpha+2\beta+2\gamma+\lambda+2\mu))\\
&+24u'(r)(2(\lambda+2\mu)+ru''(r)(\alpha+\beta+\gamma+3\lambda+6\mu))\\
&+3u'(r)^4(2(6\alpha+8\beta+5\gamma)+5r(\alpha+\beta+\gamma)u''(r)))+2r^4u(r)(8(r(\alpha+3(\beta+\lambda))u''(r)\\
&-3(\lambda+2\mu))+3(\alpha+3\beta)u'(r)^4+12(\alpha+3\beta)u'(r)^3+4u'(r)^2(5\alpha+3(6\beta+\lambda)+3r(\alpha+3\beta)u''(r))\\
&+8u'(r)(\alpha+3(\beta+\lambda)+3r(\alpha+3\beta)u''(r)))+4r^3u(r)^2(2(r(2\alpha+9\beta+3\lambda)u''(r)\\
&-3(2\alpha+4\beta+\gamma+6\lambda+6\mu))+3u'(r)^2(\alpha+6\beta+r(\alpha+3\beta)u''(r))+6r(\alpha+3\beta)u'(r)u''(r))\\
&+4r^2u(r)^3(2(-13\alpha-6(5\beta+\gamma+\lambda+\mu)+r(\alpha+6\beta)u''(r))+(\alpha+6\beta)u'(r)^2-2(\alpha+6\beta)u'(r))\\
&+2ru(r)^4(-32\alpha-72\beta-15\gamma+r(\alpha+6\beta)u''(r)-2(\alpha+6\beta)u'(r))-6u(r)^5(2\alpha+4\beta+\gamma)=0
\end{aligned}
$$

We use this nonlinear ODE to fit the pressure profile found in the experimental data using only the purely compressional third-order elastic constant $\alpha = 3.6$ Pa, leaving $\beta = \gamma = 0$. In this same fit, we set the other elastic constants $K = 0.093$ Pa and $\mu = 0.092$ Pa based on studies of hard sphere elastic constants [32]. We also set the volume change $\Delta V = -0.083$ to be the same as the experimental value. In this fit, we are able to reproduce the experimental pressure ring with one third-order elastic constant and one initial condition (u' far from the vacancy).

The value of α we find from our fit of the pressure ring is consistent with the variation of bulk modulus with packing fraction as calculated by hard sphere simulations. We can directly compare these values using the equation of state. Given the pressure of a hard sphere system as a function of packing fraction, $P(\phi)$, we can expand the elastic constants as $K(\phi_0) + K'(\phi_0)(\phi - \phi_0) + \frac{1}{2}K''(\phi_0)(\phi - \phi_0)^2 + \cdots$ giving $\alpha = K'(\phi_0) = \partial_\phi(\phi\partial_\phi P)|_{\phi_0}$. Using the functional form for $P(\phi)$ we get that $\alpha(0.59) \approx 3.0$ Pa in agreement with our fit $\alpha = 3.6$ to experimental stresses using nonlinear elasticity.

4. Vacancy interaction

The overall sign of the interaction between vacancies must be negative as vacancies are in general attracted to areas of higher pressure just as interstitials are attracted to areas of

DOI: 10.1038/NMAT4715

lower relative pressure. In the case of two vacancies, the local increase in pressure around one vacancy acts as a higher pressure region for the second, causing them to mutually attract. Physically speaking, the collapse of particles towards the core of one vacancy causes particles to collide more frequently which is relieved by the negative volume change given by the second vacancy.

The above argument gives the dominant nonlinear term (the linear field of one vacancy coupling to the nonlinear pressure around another). Higher order effects can be repulsive but are smaller than this leading order term. Specifically, to calculate the attraction or repulsion of vacancies, we look at the elastic free energy, which strictly speaking is entirely entropic. In this treatment, we will be calling all entropic contributions aside from the configurational entropy the elastic energy E_{elastic}, giving us a free energy density $\mathcal{F} = E_{\text{elastic}} - TS_{\text{conf}}$. To first order, the elastic energy density is $E_{\text{elastic}} = \sigma_{ij}\epsilon_{ij}$ where σ is stress and ϵ is strain. We consider the perturbative view of the elastic free energy in the case of the interaction of two vacancies A and B, which can be expanded into three primary terms, $E_{\text{elastic}} = \sigma_{ij}^{A,\text{L}}\epsilon_{ij}^{B,\text{L}} + 2\sigma_{ij}^{A,\text{N}}\epsilon_{ij}^{B,\text{L}} + \sigma_{ij}^{A,\text{N}}\epsilon_{ij}^{B,\text{N}}$ where L indicates a linear contribution and N indications a nonlinear one. In isotropic linear elastic theory, vacancies do not interact making the first term independent of vacancy separation and leaving us with the second and third terms of the expansion. The second term is the linear part vacancy B's quadrupole strain field sitting in the nonlinear (pressure bump) stress field of vacancy A. In this simple case, we know that the energy can be given by the vacancy quadrupole $E = \sigma_{ij}^{\text{ext}}Q_{ij}^{B}$, where the strain quadrupole for a vacancy is diagonal $Q_{ij}^{B} = \Delta V^{B}\delta_{ij}$ and $\sigma^{\text{ext}} = \sigma^{A,\text{N}}$ is an external stress field given by vacancy A. Therefore, the energy can be written $E = \sigma_{ii}^{\text{ext}}\Delta V^{B} = \sigma_{ii}^{A,\text{N}}\Delta V^{B} = P^{A,\text{N}}\Delta V^{B}$. Since $\Delta V \leq 0$ for vacancy defects, this term is negative, leading to an overall attraction, consistent with previous literature [33–36]. This calculation will have higher-order corrections due to the nonlinear elastic overlap of the nonlinear pressure rings $\propto P^{A,\text{N}}P^{B,\text{N}}$ as well as nonlinear corrections to the pressure bump itself due to the presence of a second vacancy, but the qualitative behavior remains unchanged.

IV. DISLOCATION STRESS AND STRAIN FIELDS

A. Experimental details

The dislocation is produced by templating the [100] axis on a glass coverslip at a registry 1.5% larger than the equilibrium lattice constant [37]. Particles are sedimented onto the substrate forming a single face-centered cubic crystal. As the crystal thickness reaches about 31 μm, a significant number of dislocations spontaneously nucleate and grow. We then image the three dimensional microstructure of an isolated dislocation using a confocal microscope. A schematic of these dislocations is found in the main text.

B. Simulated dislocation stresses

To closely simulate the particular dislocation studied in the experiment, we import the experimentally measured particle positions into the Brownian dynamics simulation. Prior to recording the stress, we relax the system to remove overlaps using a soft Hertzian potential and a large damping factor to ensure very little rearrangement. We then freeze the border particles as labeled in red in Fig. 10 to ensure that the topologically constrained dislocation does not migrate. After performing a time average, we find that the calculated stress field, both through virial calculation and SALSA method, are in excellent agreement with the experiment, providing a confirmation to the SALSA measurements. Importantly, since this simulation procedure only requires a single snapshot of data for the initial condition, this technique can be particularly useful in determining stresses in the experimental cases where time average is challenging. For instance, it is difficult to perform a time average in a system where the fluorescent dye photobleaches significantly or the dynamic time-scale is comparable to the time between acquisition of successive image stacks.

C. Continuum elastic theory

To compare against isotropic linear elasticity, we again calculate the stress field of the dislocation. The stress field of a dislocation in coordinates where z is along the dislocation

DOI: 10.1038/NMAT4715

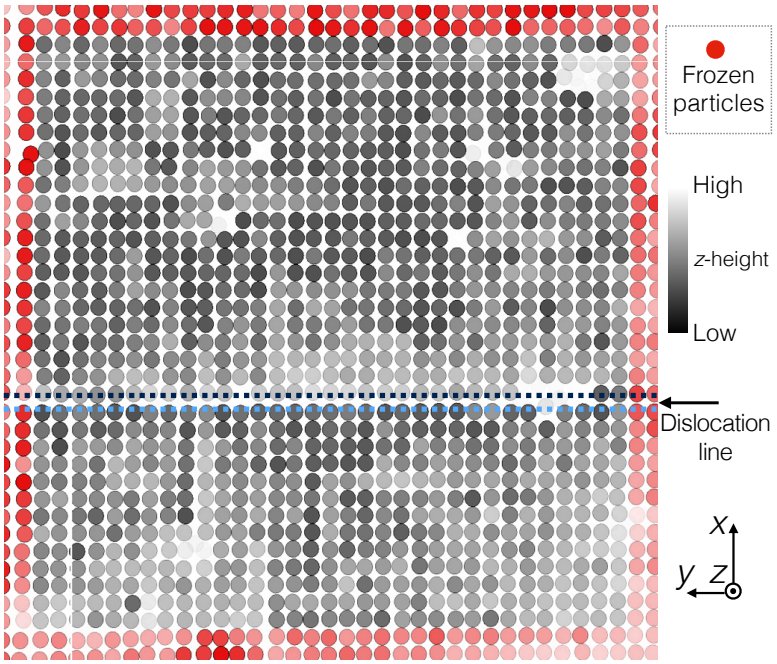

FIG. 10: **Frozen particle border (dislocation).** A screen-shot of our Brownian dynamics simulation of the experimental fcc crystal. In shades of gray are active hard sphere particles while in red are the frozen boundary particles. Luminance in this picture roughly indicates the position in the z direction with only a thin slice of the entire simulation shown and darker colors indicating being deeper into the page. The dislocation line is visible 1/3 from the bottom of the image running left to right as indicated by the discontinuity in particle shade between adjacent rows.

line, is given by [38]

$$\sigma_{xx} = -y\frac{3x^2+y^2}{(x^2+y^2)^2}$$
$$\sigma_{yy} = y\frac{x^2-y^2}{(x^2+y^2)^2}$$
$$\sigma_{xy} = x\frac{x^2-y^2}{(x^2+y^2)^2}$$
$$\sigma_{zz} = \nu(\sigma_{xx}+\sigma_{yy})$$

Using the method known as Dislocation Extraction Algorithm (DXA), we extract the line dislocation for our partial dislocation [39]. We rotate and translate the theoretical stress field for a single dislocation, integrating along the length of the dislocation as done in the

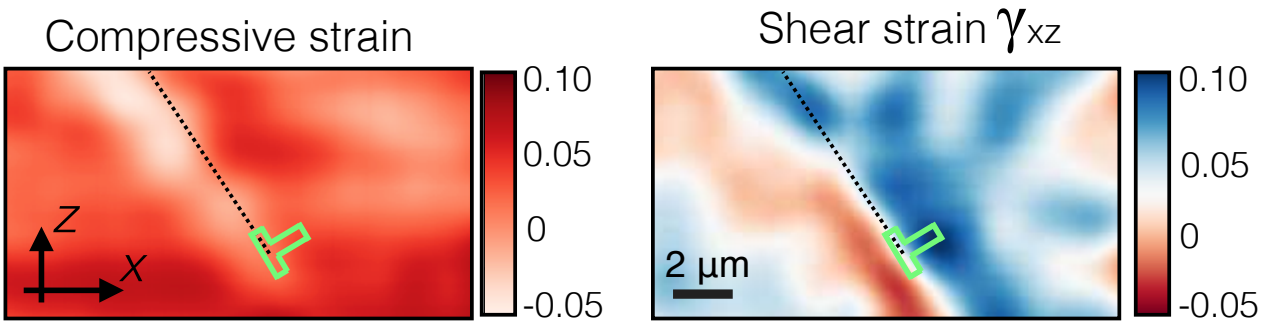

FIG. 11: **Strain fields of a dislocation.** Experimental measurements of strain using the technique of Falk *et al.* [40] showing both compressive (left) and shear (right) strain distributions near a dislocation defect. The approximate location of the dislocation core is labeled with a ($\perp$). Notice that while the trend is very similar to that of the dislocation stress field (as in linear elasticity), there is a stronger divergence towards the core which is highlighted in the main text in Fig. 3.

experiment and simulation. Doing so, we find an excellent agreement with the other methods as shown in the main text Fig 3.

D. Strain fields

To investigate the relation between stress and strain, we determine the strain field near the dislocation. Following a previously developed algorithm [40], we measure the particle-level strain by quantifying the local affine deformation of individual particles. The compressive and shear strain (γ_{xz}) fields are shown in Fig. 11. We find that the strain fields show qualitatively similar features found in the stress distributions. However, as illustrated in Fig. 3(c) of the main paper, the stress-strain curve deviates from linearity near defects where strains are large.

E. Elastic moduli

Using the strain measurement, we analyze other experimentally accessible cubic moduli as done in the main manuscript. To that end, we compute the compressive C_{33} and shear C_{13} modulus profiles and discuss their behaviors below. We focus on the moduli associated with the strain component γ_{zz}, which shows a larger response than γ_{xx} and γ_{yy} in our experiment.

DOI: 10.1038/NMAT4715

For this analysis we rotate our stress and strain tensors so that the x and y axes align with the (100) and (010) axes of the cubic system. In this frame, the moduli for an cubic crystal have the following symmetries: $C_{33} = C_{22} = C_{11}$, and $C_{23} = C_{13} = C_{12}$.

To compute the compressive modulus near the dislocation core, we first determine the compressive stress σ_{zz} and strain γ_{zz}. Here, we determine the uniform background strain (due to the overall pressure arising from confinement and gravity) by matching the measured modulus to the corresponding theoretical value [41]. We then perform the same analysis used in the shear modulus calculation, and plot the compressive modulus C_{33} as a function of position $r/2a$ in Fig. 12(a). The region of the dislocation core is at $r/2a \approx 5.5$ (gray shade). We find that C_{33} is higher on the side with an additional half plane of particles. Similarly, we also observe a reduction in C_{33} on the other side due to the missing half plane of particles. We also find that the trend of the shear modulus C_{23} is similar to the compressive modulus C_{33} (Fig. 12(b)), which shows an enhancement on the left side and a reduction on the right.

The moduli we report are only calculated along a line perpendicular to the glide plane of the dislocation. The other two natural directions along the glide plane are excluded due to experimental limitations. Along the burgers vector we are limited by the noise in the stress and strain fields. Since the modulus is the ratio of the two, zeros remain problematic, similar to issues in deconvolution, and a new method of inference must be applied to the moduli in these regions. Along the dislocation line, we have already collapsed the data by averaging the stress and strain fields in this direction in order to reduce noise in the x-z plane. This averaging makes it infeasible to calculate the modulus variation in this direction. Due to symmetry, this direction should display a constant modulus. In the future, with a full time series of dislocation images, we can begin to look at the modulus variation near kinks and jogs along the dislocation line.

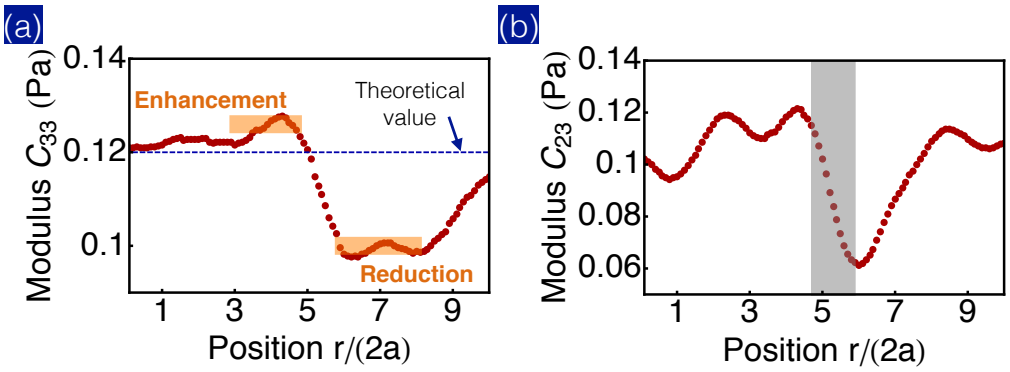

FIG. 12: Profile of the cubic moduli C_{33} and C_{23}. (a) Compressive modulus C_{33} versus position perpendicular to the glide plane of the dislocation. (b) Shear modulus C_{23} measured along the same direction. Both moduli are calculated using the protocol described in the main manuscript.

V. POLYCRYSTAL STRESS FIELDS

A. Experimental details

We show a confocal image of the polycrystal we use in our experimental analysis in Fig. 13(a). The shown field of view is the same as the one of the stress field reported in the main manuscript. We show only a slice in the x-y plane of a complete 3D image stack. The z-interval between adjacent scan slices is 0.135 μm $\sim$ 0.1 times the particle diameter. By matching the refractive indices of the water-glycerol mixture and silica particles, we minimize effects from the point spread function and z-axis spherical aberration, thus optimizing the image quality. We show the featured particle position with green circles in Fig. 13 (a). The data are visually overlaid to ensure there are no missing or repeated features.

To investigate the featuring accuracy, we plot the 1D $g(r)$ of the suspension in Fig. 13(b). As indicated by the sharpness of the first peak of $g(r)$, limiting our field of view to the first ten layers from the coverslip (in the optical z direction) enables us to accurately feature the particle positions. The spread of this peak arises from three contributions: featuring errors, polydispersity, and the thermal fluctuation of the equilibrium separation between particles. The location of the peak is primarily influenced by particle featuring errors and the packing fraction of the sample. While the polydispersity of this sample is $\sigma_a^2 \sim 5\%\langle a\rangle = 50$ nm, this variation in size will not shift the peak of $g(r)$ from the mean particle diameter (Fig. 13) unless there are spatial correlations of particle size. Therefore, at most, the averaging

DOI: 10.1038/NMAT4715

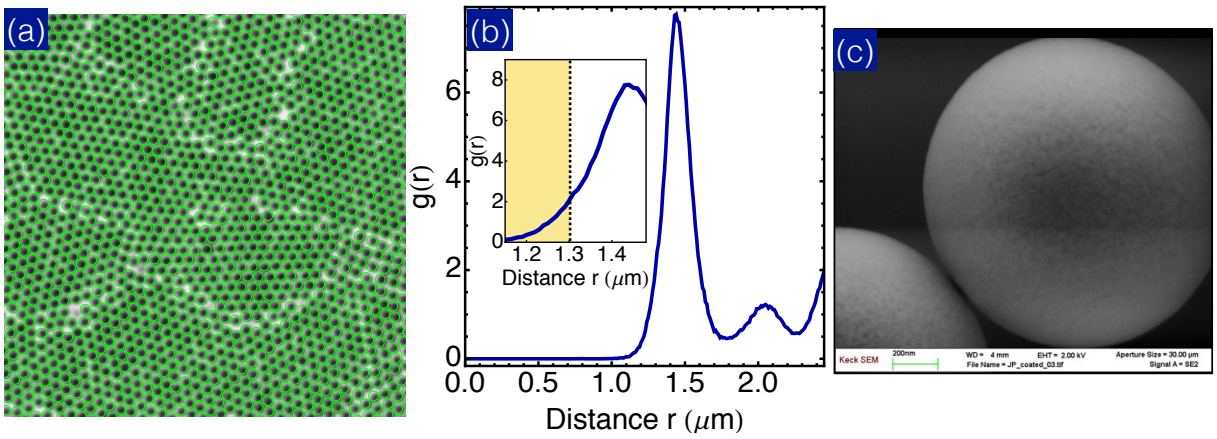

FIG. 13: **Colloidal polycrystal sample.** (a) A representative slice of a 3D confocal image stack. Green circles illustrate the featured particle positions. This overlaid image shows that all particle positions are correctly identified without any missing particles. (b) The pair correlation function $g(r)$ calculated using featured particle positions. In the inset we show that the amount of particle overlap (yellow region) is negligible. (c) A SEM micrograph of two particles showing how the true particle size was determined in the sample.

featuring errors should correspond to this peak shift of 50 nm.

Furthermore, we show a SEM micrograph to illustrate the roundness of the colloidal particles and the smoothness of their surfaces, see Fig. 13(c). As shown in the SEM image, the surface roughness is less than the SEM resolution $\sim$ 5 nm. We also use the SEM image to measure the polydispersity of the silica colloids. We find that the polydispersity of the sample is less than 3% of the particle size, consistent with the specification provided by the manufacturer.

In the stress measurement of the polycrystal, we average the calculated stress field over 50 stacks of images. The structure of the polycrystal remains unchanged within the acquisition time ($\sim$ 30 s). While we expect to observe short-time stress fluctuations arising from particle Brownian motion within the acquisition time, we do not find any significant stress fluctuations on longer time scales.

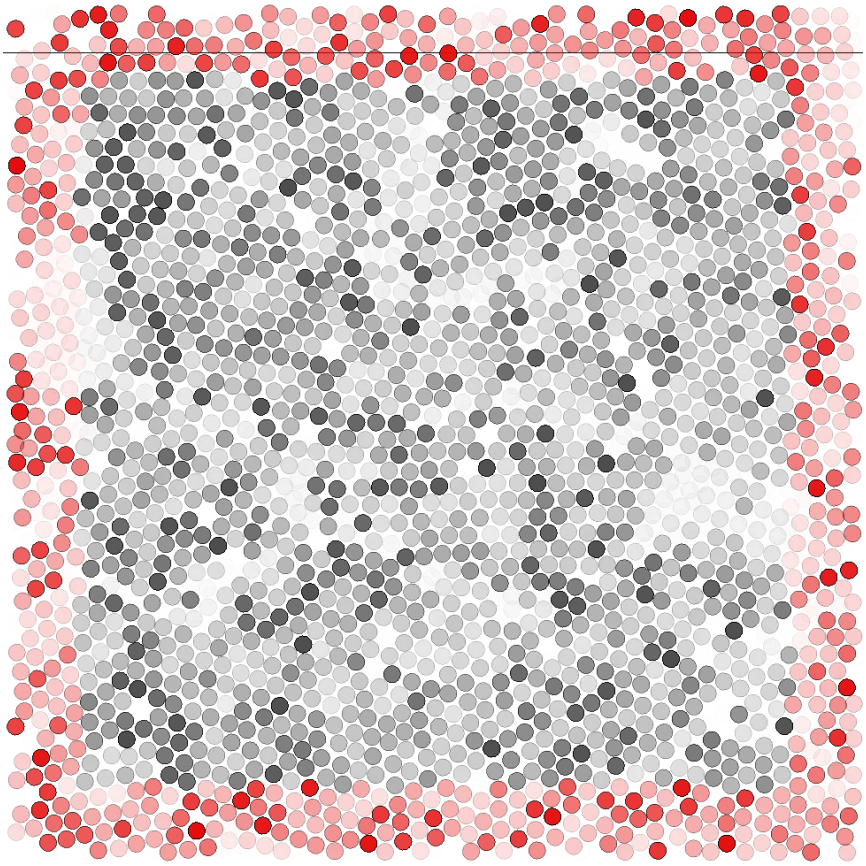

FIG. 14: **Frozen particle border (polycrystal).** A screen-shot of our Brownian dynamics simulation of the experimental polycrystal. In shades of gray are active hard sphere particles while in red are the frozen boundary particles. Luminance in this picture roughly indicates the position in the z direction with only a thin slice of the entire simulation shown.

B. Simulated polycrystal stresses

As with the dislocation stresses, we verified that the experimental stresses are accurate using a simulation-experiment hybrid. Again we use the experimentally featured particle positions as initial conditions for our hard sphere Brownian dynamics simulation. For each experimental snapshot, we remove overlaps and freeze boundary particles as before, then evolve the system, measuring stresses using both the true virial measurements as well as SALSA. By averaging over the various snapshots, we arrive at a stress field very similar to that found by the experimental SALSA calculation.

DOI: 10.1038/NMAT4715

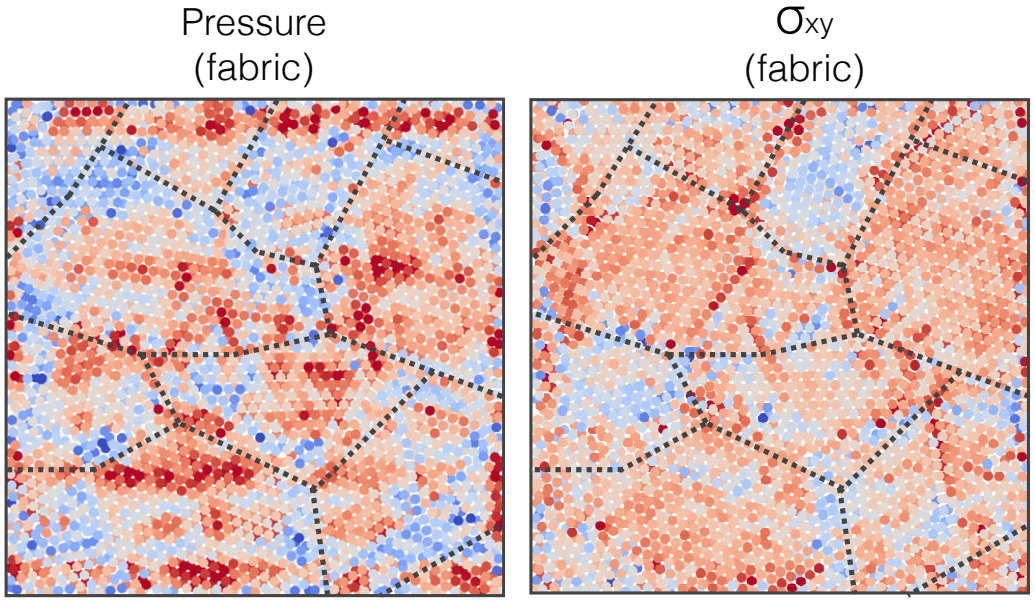

FIG. 15: **Per-particle virials** The experimental polycrystal with particles colored by the magnitude of the fabric tensor (directly proportional to particle virial). While we see large scale correlations of fabric tensor trace with grain interiors and variation of off-diagonal components between grains, the magnitude of variation is much smaller than that found in previous numerical studies of stress distributions in strained polycrystals [14]

C. Virial stresses

In simulation literature, the atomic-level stress has been referred to as the virial of an individual atom either normalized or un-normalized by the system volume [14, 42–44]. Here, the virial $F_i x_j$ can be considered to be a stress that does not account for the local variation of atomic (particle) free volume. To compare our experimental results with the previous simulation findings (which do not correct for local particle density fluctuations), we plot (Fig. 15) the un-smoothed fabric tensor (local structural anisotropy) that is calculated using SALSA. For detailed information of the fabric tensor calculation, see the section of SALSA derivation. As shown in Fig. 15, we find that both the pressure and shear stress fluctuations are evenly distributed throughout the polycrystal. This is in sharp contrast to simulation results of sheared atomic polycrystals [14], which showed much stronger virial fluctuations at grain boundaries than in grain interiors.

[1] John F Brady. The rheological behavior of concentrated colloidal dispersions. *J. Chem. Phys.*, 99(July):567–581, 1993.

[2] Jean-Pierre Hansen and Ian R McDonald. *Theory of simple liquids*. Elsevier, 1990.

[3] Erik Lange, Jose B Caballero, Antonio M Puertas, and Matthias Fuchs. Comparison of structure and transport properties of concentrated hard and soft sphere fluids. *The Journal of chemical physics*, 130(17):174903, 2009.

[4] David R Foss and John F Brady. Brownian dynamics simulation of hard-sphere colloidal dispersions. *Journal of Rheology (1978-present)*, 44(3):629–651, 2000.

[5] WCK Poon. The physics of a model colloid–polymer mixture. *Journal of Physics: Condensed Matter*, 14(33):R859, 2002.

[6] D Rosenbaum, PC Zamora, and CF Zukoski. Phase behavior of small attractive colloidal particles. *Physical review letters*, 76(1):150, 1996.

[7] VERONIQUE Trappe, V Prasad, Luca Cipelletti, PN Segre, and DAVID A Weitz. Jamming phase diagram for attractive particles. *Nature*, 411(6839):772–775, 2001.

[8] Klaus Zahn, Axel Wille, Georg Maret, Surajit Sengupta, and Peter Nielaba. Elastic properties of 2d colloidal crystals from video microscopy. *Physical review letters*, 90(15):155506, 2003.

[9] Anand Yethiraj and Alfons van Blaaderen. A colloidal model system with an interaction tunable from hard sphere to soft and dipolar. *Nature*, 421(6922):513–517, 2003.

[10] Kerstin N Nordstrom, E Verneuil, PE Arratia, Anindita Basu, Zheng Zhang, Arjun G Yodh, Jerry P Gollub, and Douglas J Durian. Microfluidic rheology of soft colloids above and below jamming. *Physical review letters*, 105(17):175701, 2010.

[11] Ke Chen, Wouter G Ellenbroek, Zexin Zhang, Daniel TN Chen, Peter J Yunker, Silke Henkes, Carolina Brito, Olivier Dauchot, Wim Van Saarloos, Andrea J Liu, et al. Low-frequency vibrations of soft colloidal glasses. *Physical review letters*, 105(2):025501, 2010.

[12] TJ Delph. Local stresses and elastic constants at the atomic scale. *Proceedings of the Royal Society A: Mathematical, Physical and Engineering Science*, 461(2058):1869–1888, 2005.

[13] V. a. Levashov, J. R. Morris, and T. Egami. Viscosity, Shear Waves, and Atomic-Level Stress-Stress Correlations. *Phys. Rev. Lett.*, 106(11):115703, March 2011.

[14] Jakob Schiøtz, Francesco D Di Tolla, and Karsten W Jacobsen. Softening of nanocrystalline

metals at very small grain sizes. *Nature*, 391(6667):561–563, 1998.

[15] Ellad B Tadmor and Ronald E Miller. *Modeling materials: continuum, atomistic and multi-scale techniques*. Cambridge University Press, 2011.

[16] AI Murdoch and D Bedeaux. Continuum equations of balance via weighted averages of microscopic quantities. *Proceedings of the Royal Society of London A: Mathematical, Physical and Engineering Sciences*, 445(1923):157–179, 1994.

[17] A Ian Murdoch. A critique of atomistic definitions of the stress tensor. *Journal of Elasticity*, 88(2):113–140, 2007.

[18] Robert J Hardy. Formulas for determining local properties in molecular-dynamics simulations: Shock waves. *The Journal of Chemical Physics*, 76(1):622–628, 1982.

[19] Ted Belytschko, Yury Krongauz, Daniel Organ, Mark Fleming, and Petr Krysl. Meshless methods: an overview and recent developments. *Computer methods in applied mechanics and engineering*, 139(1):3–47, 1996.

[20] See-Eng Phan, William B Russel, Zhengdong Cheng, Jixiang Zhu, Paul M Chaikin, John H Dunsmuir, and Ronald H Ottewill. Phase transition, equation of state, and limiting shear viscosities of hard sphere dispersions. *Physical Review E*, 54(6):6633, 1996.

[21] Xiang Cheng, Jonathan H McCoy, Jacob N Israelachvili, and Itai Cohen. Imaging the microscopic structure of shear thinning and thickening colloidal suspensions. *Science*, 333(6047):1276–9, September 2011.

[22] Neil YC Lin, Sushmit Goyal, Xiang Cheng, Roseanna N Zia, Fernando A Escobedo, and Itai Cohen. Far-from-equilibrium sheared colloidal liquids: Disentangling relaxation, advection, and shear-induced diffusion. *Physical Review E*, 88(6):062309, 2013.

[23] Alejandro Torres-Sánchez, Juan M Vanegas, and Marino Arroyo. Examining the mechanical equilibrium of microscopic stresses in molecular simulations. *Physical review letters*, 114(25):258102, 2015.

[24] Colin JR Sheppard, Min Gu, Keith Brain, and Hao Zhou. Influence of spherical aberration on axial imaging of confocal reflection microscopy. *Applied optics*, 33(4):616–624, 1994.

[25] Colin JR Sheppard and Min Gu. Aberration compensation in confocal microscopy. *Applied optics*, 30(25):3563–3568, 1991.

[26] P Török, SJ Hewlett, and P Varga. The role of specimen-induced spherical aberration in confocal microscopy. *Journal of microscopy*, 188(2):158–172, 1997.

[27] Thijs Herman Besseling, Jissy Jose, and A BLAADEREN. Methods to calibrate and scale axial distances in confocal microscopy as a function of refractive index. *Journal of microscopy*, 257(2):142–150, 2015.

[28] Neil YC Lin, Jonathan H McCoy, Xiang Cheng, Brian Leahy, Jacob N Israelachvili, and Itai Cohen. A multi-axis confocal rheoscope for studying shear flow of structured fluids. *Review of Scientific Instruments*, 85(3):033905, 2014.

[29] Peter J Shaw and David J Rawlins. The point-spread function of a confocal microscope: its measurement and use in deconvolution of 3-d data. *Journal of Microscopy*, 163(2):151–165, 1991.

[30] Wilson CK Poon, Eric R Weeks, and C Patrick Royall. On measuring colloidal volume fractions. *Soft Matter*, 8(1):21–30, 2012.

[31] Rei Kurita, David B Ruffner, and Eric R Weeks. Measuring the size of individual particles from three-dimensional imaging experiments. *Nature communications*, 3:1127, 2012.

[32] Sander Pronk and Daan Frenkel. Large difference in the elastic properties of fcc and hcp hard-sphere crystals. *Physical review letters*, 90(25):255501, 2003.

[33] Wolfgang Lechner and Christoph Dellago. Defect interactions in two-dimensional colloidal crystals: vacancy and interstitial strings. *Soft Matter*, 5(14):2752–2758, 2009.

[34] Wolfgang Lechner and Christoph Dellago. Point defects in two-dimensional colloidal crystals: simulation vs. elasticity theory. *Soft Matter*, 5(3):646–659, 2009.

[35] Fabio Cinti, Tommaso Macrì, Wolfgang Lechner, Guido Pupillo, and Thomas Pohl. Defect-induced supersolidity with soft-core bosons. *Nature communications*, 5, 2014.

[36] CH Bennett and BJ Alder. Studies in molecular dynamics. ix. vacancies in hard sphere crystals. *The Journal of Chemical Physics*, 54(11):4796–4808, 1971.

[37] Peter Schall, Itai Cohen, David A Weitz, and Frans Spaepen. Visualization of dislocation dynamics in colloidal crystals. *Science*, 305(5692):1944–1948, 2004.

[38] Derek Hull and David J Bacon. *Introduction to dislocations*, volume 37. Elsevier, 2011.

[39] Alexander Stukowski and Karsten Albe. Extracting dislocations and non-dislocation crystal defects from atomistic simulation data. *Modelling and Simulation in Materials Science and Engineering*, 18(8):085001, 2010.

[40] ML Falk and JS Langer. Dynamics of viscoplastic deformation in amorphous solids. *Physical Review E*, 57(6):7192, 1998.

DOI: 10.1038/NMAT4715

[41] Daan Frenkel and Anthony JC Ladd. Elastic constants of hard-sphere crystals. *Physical review letters*, 59(10):1169, 1987.

[42] Valentin A Levashov, James R Morris, and Takeshi Egami. Viscosity, shear waves, and atomic-level stress-stress correlations. *Physical review letters*, 106(11):115703, 2011.

[43] C Mottet, G Rossi, F Baletto, and R Ferrando. Single impurity effect on the melting of nanoclusters. *Physical review letters*, 95(3):035501, 2005.

[44] Kenji Yoshimoto, Tushar S Jain, Kevin Van Workum, Paul F Nealey, and Juan J de Pablo. Mechanical heterogeneities in model polymer glasses at small length scales. *Physical review letters*, 93(17):175501, 2004.

[45] There is a nomenclature problem when describing the stress and strain around a point defect. Some describe them as quadrupolar fields, reflecting the similar $\cos 2\theta$ angular dependence with electrical quadrupoles. This angular dependence is special, however, to isotropic elastic theory; also, the displacement field has a 'monopolar' isotropic component $\Delta V/(4\pi r^2)$ with no angular dependence. (However, as noted in Fig. 3, the off-diagonal stresses for an isotropic vacancy still look like quadrupoles.) Some describe them as elastic dipoles, reflecting both the common $1/r^3$ force law with electric dipoles and their origins as 'force dipoles' (two opposite forces acting on nearby points in the elastic medium.) Finally, others (particularly studying elasticity in amorphous systems) name the field after Eshelby – thus bypassing the choice by using an uninformative label. Here, we use the term quadrupole, mostly because the 'strength' of a point defect is quantified by a 3x3 symmetric matrix (either the strain quadrupole Q_{ij} described here, or the corresponding stress quadrupole / force dipole.) We must note, however, that in the present case of vacancies in a cubic environment, $Q_{ij} = \Delta V \delta_{ij}$ has no correspondence to electric quadrupoles, which are traceless.